Nanoscale Advances

ROYAL SOCIETY OF CHEMISTRY

PAPER

View Article Online
View Journal | View Issue

Cite this: *Nanoscale Adv.*, 2023, **5**, 2756

Morphological dependent exciton dynamics and thermal transport in $MoSe_2$ films†

Jay Deep Gupta, Priyanka Jangra, Bishnu Pada Majee and Ashish Kumar Mishra *

Thermal transport and exciton dynamics of semiconducting transition metal dichalcogenides (TMDCs) play an immense role in next-generation electronic, photonic, and thermoelectric devices. In this work, we synthesize distinct morphologies (snow-like and hexagonal) of a trilayer $MoSe_2$ film over the SiO_2/Si substrate *via* the chemical vapor deposition (CVD) method and investigated their morphological dependent exciton dynamics and thermal transport behaviour for the first time to the best of our knowledge. Firstly, we studied the role of spin–orbit and interlayer couplings both theoretically as well as experimentally *via* first-principles density functional theory and photoluminescence study, respectively. Further, we demonstrate morphological dependent thermal sensitive exciton response at low temperatures (93–300 K), showing more dominant defect-bound excitons (E_L) in snow-like $MoSe_2$ compared to hexagonal morphology. We also examined the morphological-dependent phonon confinement and thermal transport behaviour using the optothermal Raman spectroscopy technique. To provide insights into the nonlinear temperature-dependent phonon anharmonicity, a semi-quantitative model comprising volume and temperature effects was used, divulging the dominance of three-phonon (four-phonon) scattering processes for thermal transport in hexagonal (snow-like) $MoSe_2$. The morphological impact on thermal conductivity (k_s) of $MoSe_2$ has also been examined here by performing the optothermal Raman spectroscopy, showing $k_s \sim 36 \pm 6$ W m^{-1} K^{-1} for snow-like and $\sim 41 \pm 7$ W m^{-1} K^{-1} for hexagonal $MoSe_2$. Our research will contribute to the understanding of thermal transport behaviour in different morphologies of semiconducting $MoSe_2$, finding suitability for next-generation optoelectronic devices.

Received 15th March 2023
Accepted 11th April 2023

DOI: 10.1039/d3na00164d

rsc.li/nanoscale-advances

Introduction

Recently, atomically thin layered structures of transition metal dichalcogenides (TMDCs) have provided extraordinary deliberation in research interest due to their unique electronic, optical, chemical, and thermal properties with high crystal quality. Unlike graphene, TMDCs nanostructures show tunable bandgap in the region of 1–2 eV, which makes them suitable for low-dimension semiconductors based on next-generation photonic and optoelectronic devices. In comparison to other conventional semiconductors, TMDCs are easy to integrate with various substrates due to their dangling bond-free interface and atomically thin structures. High-quality 2D TMDCs have low interface scattering, high charge carrier mobility, and outstanding electronic performance.[1,2] Additionally, 2D TMDCs materials also delivered a new approach for quantum emitters to study the quantum physical phenomena such as quantum entanglement between phonon and photon. In recent years, there have been few efforts to demonstrate TMDCs as single-photon emitters (SPEs) by creating defect states.[3,4] Among 2D TMDCs, the less-explored molybdenum diselenide ($MoSe_2$) is expected to be one of the most imperative and superior candidates for optoelectronic behaviour due to its high optical absorbance of ~10% (775 nm) to 30% (476 nm), low direct bandgap (~1.58 eV) and good photoactivity, making it suitable for phototransistor, photovoltaic single-junction solar cells, photocatalysis, and photoelectrochemical cells.[5,6] Theoretical and experimental investigations of $MoSe_2$ are being explored for atomically thin spintronic and valleytronic devices due to its spin-splitting energy at the top of the valence band.[7,8]

Among different methods such as mechanical/chemical exfoliations, chemical vapor deposition (CVD), and physical methods such as sputtering/pulsed laser deposition involving physical deposition of atoms, ions, or molecules on a substrate, the CVD technique can generate large areas of thin films of $MoSe_2$ with and without intrinsic defects.[9] This defect tunability in CVD-grown $MoSe_2$ can be utilized for the development of new quantum light sources such as SPEs, flexible nano-electronics, and optoelectronic devices.[10,11] Integrated electronic circuits,

School of Materials Science and Technology, Indian Institute of Technology (Banaras Hindu University), Varanasi-221005, India. E-mail: akmishra.mst@iitbhu.ac.in

† Electronic supplementary information (ESI) available: Density functional studies, configurational coordinate diagram, FWHM of temperature-dependent PL, temperature-dependent Raman spectra, power-dependent Raman spectra, calculations of laser spot size at different objective lenses, calculation of α_a value for trilayer $MoSe_2$. See DOI: https://doi.org/10.1039/d3na00164d

made with millions of transistors, generate excess heat during operation, which affects the performance and stability, leading to the probable failure of the device. Hence, it is important to understand the thermal transport behaviour of $MoSe_2$ for the development of its devices. The thermal behaviour of $MoSe_2$ can be explained by the exchange of phonon–electron interaction and vibrational properties, where heat can be transferred due to the transport of electrons and phonons.[12] Kandemir *et al.* predicted the thermal conductivity of $MoSe_2$ crystal in the range 75 to 25 W m^{-1} K^{-1} at different temperatures between 200 and 500 K using molecular dynamics (MD) simulation.[13] Hong *et al.* predicted the thermal conductivities of 43.88 ± 1.33 and 41.63 ± 0.66 W m^{-1} K^{-1} for armchair and zigzag directions of $MoSe_2$, respectively, using classical nonequilibrium MD simulation study.[14] Zobeiri *et al.* performed the frequency-resolved energy transport technique to investigate the in-plane thermal conductivity of different thicknesses of suspended $MoSe_2$ samples. They observed that the thermal conductivity value increased from 6.2 ± 7.7 to 25.7 ± 7.7 W m^{-1} K^{-1} with varying thicknesses from 5 to 80 nm.[15] Zhang *et al.* chose the opto-thermal Raman technique to determine the thermal transport properties of mechanically exfoliated $MoSe_2$ and observed the thermal conductivities of 59 ± 18 and 42 ± 13 W m^{-1} K^{-1} for monolayer and bilayer $MoSe_2$, respectively.[16] Recently, Sun *et al.* determined the thermal conductivity of polycrystalline $MoSe_2$ to be around 28.48 W m^{-1} K^{-1}, suspended on a gold substrate.[17] These studies on the thermal conductivity of $MoSe_2$ are predicted either theoretically or mechanically exfoliated $MoSe_2$, which are good for fundamental understanding but not for real application in devices.

Morphological-dependent exciton dynamics and thermal transport studies of CVD-grown $MoSe_2$ are still missing in the literature. Here, we studied the morphological-dependent exciton dynamics of CVD-grown snow-like and hexagonal $MoSe_2$ film over SiO_2/Si substrate at low temperatures using the temperature-dependent photoluminescence studies, showing contrasting exciton behaviour of two morphologies. We also demonstrate the linear and non-linear thermal transport behaviour along with thermal conductivity and interfacial thermal conductance for snow-like and hexagonal $MoSe_2$ using the optothermal Raman spectroscopy technique. To the best of our knowledge, this is the first time, we are reporting the morphological dependent exciton dynamics and thermal transport properties of the CVD-grown $MoSe_2$ film.

Experimental and computational details

Synthesis of the $MoSe_2$ film

The snow-like and hexagonal morphologies of $MoSe_2$ film over the SiO_2/Si substrate were grown using the CVD process. Selenium (Se) and molybdenum trioxide (MoO_3) powder were used as precursors with SiO_2/Si as a substrate in a two-zone furnace. The substrate was initially cleaned with piranha solution, washed with DI water and isopropanol (IPA), and then sonicated in acetone for 15 minutes. A quartz boat containing 15 mg of MoO_3 was placed in a zone-1 with the SiO_2/Si substrate on top of the boat. In zone-2, the second quartz boat was placed with 150 mg of Se powder. A vacuum was produced and successive purging of Ar gas with 10% H_2 was performed to remove the residual oxygen from the reaction chamber. Zones 1 and 2 were heated to temperatures of 750 °C and 300 °C, respectively, for the synthesis of the $MoSe_2$ film. Over the course of a 15 minute reaction time, the Ar/H_2 was set at 50 sccm. The system was cooled down quickly after finishing the reaction process.

Characterization of the $MoSe_2$ film

The shape and lateral dimensions of the grown film were initially observed using an optical microscope (Nikon Eclipse LV150N). The thickness and surface topography of $MoSe_2$ were determined using an atomic force microscope (AFM type NT-MDT, Russia). A micro-Raman spectrometer (STR-300, Arix Corporation) with a 532 nm excitation source was used to conduct the Raman and PL measurements. The temperature and power-dependent Raman measurements were performed using 100× and LWD 50× objective lenses and a grating of 2400 grooves per mm with a spectral resolution of 0.4 cm^{-1} and a Linkam thermal stage (HFS600E).

Computational details

Theoretical calculations were performed for trilayer $MoSe_2$ by density functional theory using QUANTUM ESPRESSO. The exchange–correlation potential was depicted by Perdew–Burke–Ernzerhof (PBE) within generalized gradient approximation (GGA) formalism. The unit cell for $MoSe_2$ was modelled in the form of supercells by applying a vacuum of 15 Å to prevent adjacent layer interaction beyond three layers along the *z*-direction. A kinetic energy cut-off for plane wave expansion and charge density were 85 Ry and 510 Ry, respectively. Initially, the structure was optimized up to minimum energy, until the total energy attains the value order of 10^{-4} Ry and then self-consistent field calculations for band structure including spin–orbit coupling among all atoms were performed. The van der Waals interaction merges in our calculation by using the Grimme-D2 correction. The Fermi level was set at 0 eV for all calculations.

Results and discussion

Growth of the $MoSe_2$ film and morphological analysis

The schematic diagram of the thermal CVD process for the growth of the $MoSe_2$ nanostructure film over the SiO_2/Si substrate is shown in Fig. S1a of the ESI.† As suggested in the literature,[18] the CVD growth process of $MoSe_2$ follows below eqn (1) and (2)-

$$MoO_3 + \frac{n}{2}Se \rightarrow MoO_{3-n} + \frac{n}{2}SeO_2 \quad (1)$$

$$MoO_{3-n} + \frac{7-n}{2}Se \rightarrow MoSe_2 + \frac{3-n}{2}SeO_2 \quad (2)$$

The first reaction mainly occurs during the ramp-up temperature and the second reaction occurs in a constant

temperature range, which is called the epitaxial process. The evolution of different morphologies in the CVD process depends upon various parameters such as the vapor pressure of precursors, reaction temperature, chemical potential, and distance between the precursors and substrate. The atomic ratio of Mo : Se controls the final morphologies of the $MoSe_2$ nanostructure. As reported in the literature,[19,20] a large number of nucleation sites as $MoO_{3-n}Se_n$ are formed initially on the surface of the substrate, and thereafter the interfacial growth of $MoSe_2$ nanostructure takes place and different morphologies evolve depending upon Mo : Se ratio. When the stoichiometric ratio of Mo and Se is 1 : 2, then the hexagonal shape is formed. Whereas, when the ratio of Mo : Se is greater than 1 : 2, the initially truncated triangles with Mo-terminated edges are formed and with rate limiting selenization snow-like structure is formed, as shown schematically in Fig. S1b–d of the ESI.† We examined the morphology of the prepared $MoSe_2$ film using optical microscopy and atomic force microscopy (AFM) techniques. The optical images of the grown snow-like and hexagonal $MoSe_2$ nanostructure films over the SiO_2/Si substrate are shown in Fig. 1a and d, respectively. Fig. 1a clearly indicates the sharp edges formed in a snow-like structure, which are absent in hexagonal-shaped $MoSe_2$. AFM studies also confirmed the same morphologies of the prepared $MoSe_2$ film (Fig. 1b and e) and the height profile (Fig. 1c and f) study showed a thickness of around 2.4 and 2.3 nm for snow-like and hexagonal morphology, respectively. The thickness of the monolayer $MoSe_2$ is around 0.7 nm based on crystallographic orientation,[21] hence, the thickness of our film clearly indicates the formation of trilayer (3L) snow-like and hexagonal $MoSe_2$ film. To examine the phase of the prepared $MoSe_2$ film, we characterized it using Raman spectroscopy. Fig. 1g shows the Lorentzian fitted Raman spectra of snow-like and hexagonal 3L-$MoSe_2$, indicating the presence of A_{1g} mode around 240.9 and 240 cm^{-1}, respectively,

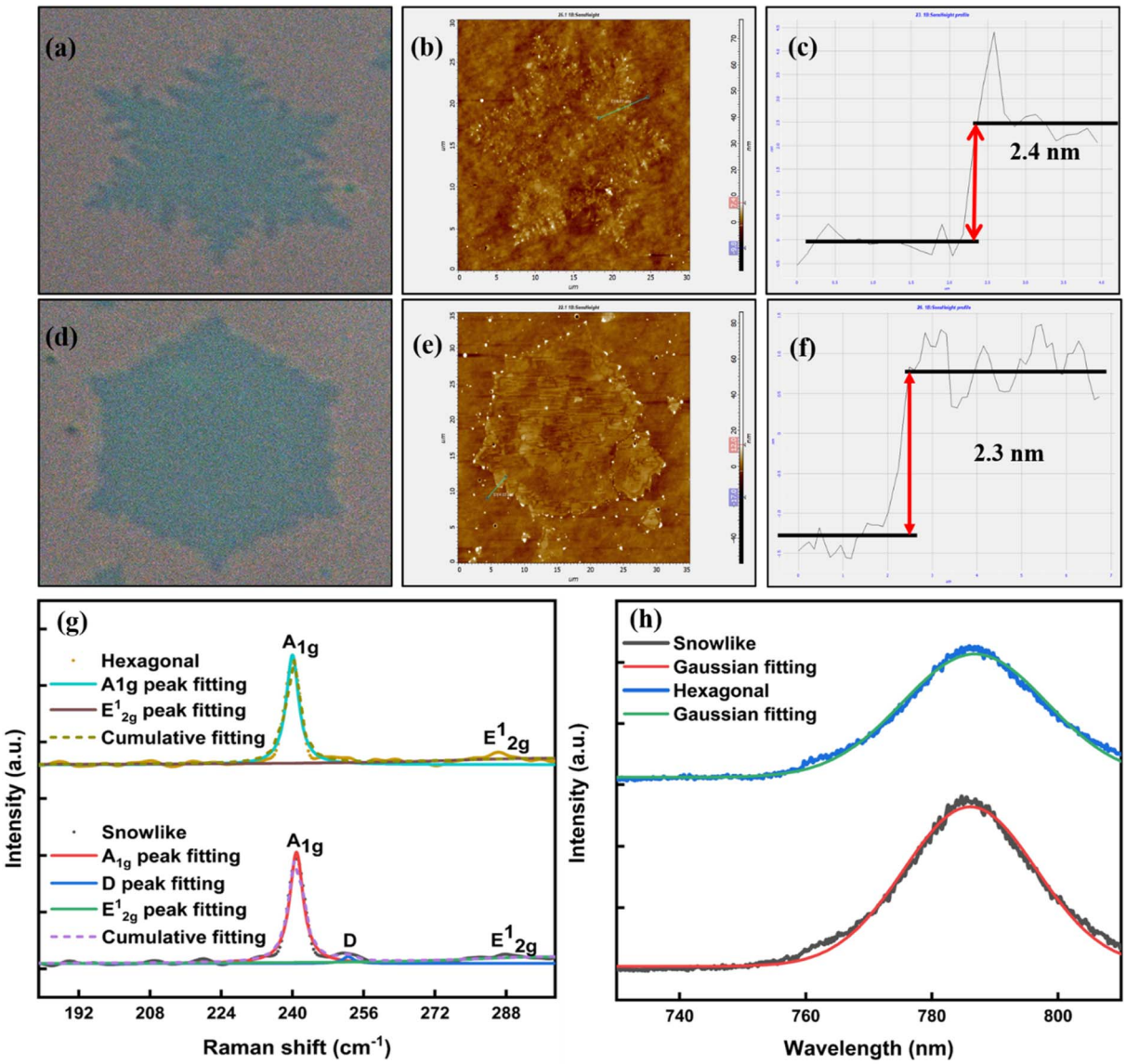

Fig. 1 (a and d) Optical images, (b and e) AFM images, and (c and f) corresponding height profiles of snow-like and hexagonal $MoSe_2$ grown over SiO_2/Si substrate; (g) room temperature Raman spectra (Lorentzian fitting of A_{1g} mode); and (h) PL spectra for snow-like and hexagonal $MoSe_2$.

which represents out-of-plane plane vibrations of Se atoms in $MoSe_2$. The broad and low intense peak at higher wavenumbers of 287.4 and 286.8 cm^{-1} is observed for snow-like and hexagonal, respectively, corresponding to the E^1_{2g} mode associated with the in-plane vibrations of Mo and Se atoms.[22] The presence of these peaks clearly indicates the formation of the 2H phase of $MoSe_2$. Interestingly, an additional peak at ~252.5 cm^{-1} was observed in snow-like nanostructure, which is usually associated with some kind of lattice disorder and/or Se vacancies by thermal annealing and hydrogen etching in the CVD process.[23] Moreover, Raman mapping was performed to examine the distribution of defects in snow-like and hexagonal $MoSe_2$, as shown in Fig. S2 of the ESI.† It clearly shows the uniform distribution of defects in snow-like $MoSe_2$ and the absence of defects throughout the region in hexagonal $MoSe_2$. Further, the semiconducting behaviour of the prepared film was examined using the PL spectroscopy technique. The Gaussian fitted room temperature PL spectra of the synthesized $MoSe_2$ film are depicted in Fig. 1h, showing similar PL emissions for both morphologies. The exciton transition at the *K*-valley of the Brillouin zone of $MoSe_2$ is the origin of the prominent peak for snow-like and hexagonal-shaped $MoSe_2$ at approximately 1.57 and 1.58 eV, respectively.[24] The strong PL emission clearly indicates the presence of direct bandgap in the prepared $MoSe_2$ film, which can be suitable for optoelectronic applications.

Density functional study

Since the synthesized film of $MoSe_2$ consists of three layers, hence we have performed the density functional theory (DFT) calculations to obtain the electronic band structure and theoretically estimate the band gap of 3L-$MoSe_2$ at 0 K, which can be confirmed experimentally by the temperature-dependent PL study of the prepared $MoSe_2$ film. The lattice structure of $MoSe_2$ contains one Mo atom sandwiched between two chalcogen atoms as shown in Fig. 2a, representing the top and side view of $MoSe_2$, while Fig. 2b shows the unit cell of $MoSe_2$. Successive layers are stacked one by one in such a way that the Mo atom is lined up with the Se atom of the next layer to generate a multilayer system and these layers interact *via* weak van der Waals forces. We used a 12 × 12 × 1 Monkhorst–Pack of *K*-points grids with path Γ–*M*–*K*–Γ of high symmetry points in the Brillouin zone for electronic band structure calculations. Fig. 2c and d show the electronic band structure and density of states, respectively, for 3L-$MoSe_2$. We observed the lowest indirect bandgap of ~0.98 eV for 3L-$MoSe_2$, which matches well with the literature.[25,26] The spin–orbit coupling effect shows a significant effect on the band structure and structural symmetry of a particular system. The energy levels at the *K*-point of the valence band and the Λ-point of the conduction band are corresponding to $d_{x^2-y^2}$ and d_{xy} orbitals of Mo atoms where the effect of spin–orbit coupling is very significant as compared to the energy levels corresponding to d_{z^2} orbitals at Γ-point of the valence band and *K*-point of the conduction band. Fig. 2d shows the density of states (DOS) *versus* energy plot indicating the bandgap of 0.98 eV between the conduction band and valence band, which are generated by the hybridization of Mo-4d and Se-4p orbitals.

The spin–orbit coupling leads to the splitting of the valence band at the *K*-point resulting in the formation of high energy (E_H) and low energy (E_L) excitons. It was theoretically

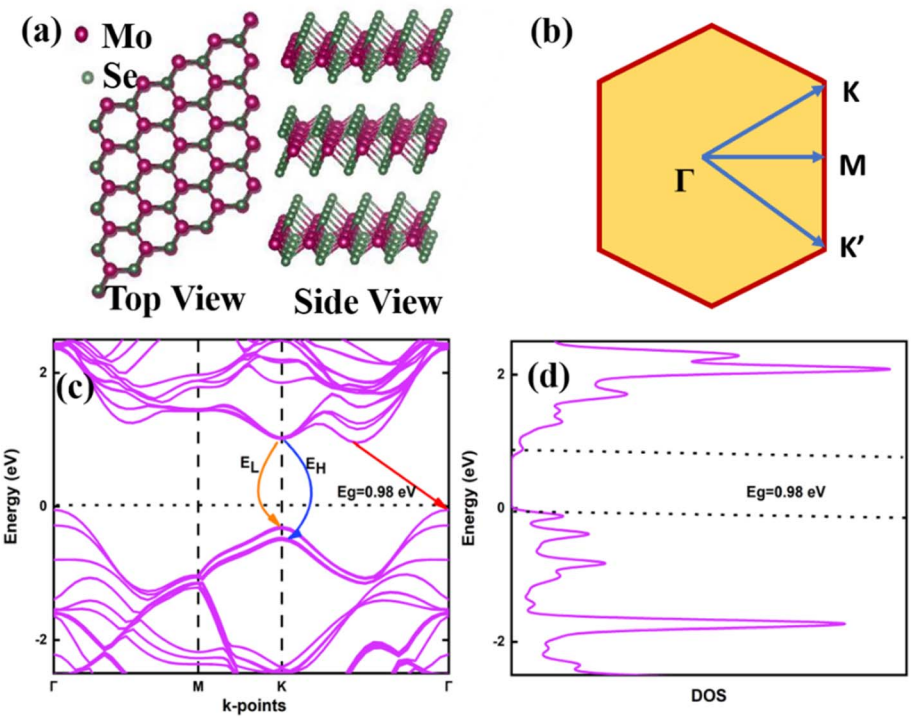

Fig. 2 (a) Top and side view of 3L-$MoSe_2$; (b) the 2D first BZ with high-symmetry points; (c) electronic band structure and (d) density of states for 3L-$MoSe_2$.

demonstrated in the literature for molybdenum-based TMDCs that the energy separation between splitting energy levels at *K*-point is always positive, resulting in the low energy excitons (E_L) as bright and high energy excitons (E_H) as dark ones.[27] Our theoretically calculated electronic band structure for 3L-$MoSe_2$ shows the energy separation between dark and bright exciton around 0.184 eV due to the spin–orbit coupling. The interlayer coupling breaks the degeneracy of the energy level at the *K*-point. In 3L-$MoSe_2$, the combination of interlayer and spin–orbit couplings results in the splitting of valence and conduction bands at the *K*-point because of the absence of inversion symmetry, as shown in Fig. S3 of ESI.†

Temperature-dependent PL study

To understand the thermal sensitive exciton behaviour of the prepared semiconducting $MoSe_2$ film, we performed a temperature-dependent PL study in the temperature range 93–300 K for both morphologies (snow-like and hexagonal) of $MoSe_2$. Fig. 3a and d show the Gaussian-fitted PL spectra for snow-like and hexagonal-shaped $MoSe_2$ films, respectively at different temperatures. The room temperature PL spectra for both morphologies indicate the existence of high energy excitons (E_H), which are blue-shifted at lower temperatures. The intensity of high-energy excitons increases at lower temperatures due to reduced non-radiative transitions *via* electron–phonon and phonon–phonon scatterings for both morphologies of $MoSe_2$. Interestingly, we observed an additional feature when the surrounding temperature of $MoSe_2$ film reached down to 213 K, a weak low-energy exciton peak (E_L) appeared at lower energy for both morphologies. As per literature reports, the defect-bound excitons are the origin of this low-energy exciton peak at low temperatures.[28] This low-energy exciton also follows the same trend as a high-energy exciton, *i.e.*, it is blue-shifted and its intensity increases at lower temperatures, as observed in Fig. 3a and d. The binding energy of the defect-bound excitons for the prepared $MoSe_2$ film was found to be 31–33 meV, lower than the high energy exciton at low temperatures, as suggested in the literature.[29] Moreover, it was found that when the temperature was lowered to 123 K, the proportional intensities of E_H and E_L are in contrast for the snow-like and hexagonal $MoSe_2$ films. It clearly showed that the defect-bound excitons (E_L) are more dominant in snow-like $MoSe_2$ compared to those in hexagonal $MoSe_2$, which can be attributed to the presence of additional Se vacancies as defects in a snow-like $MoSe_2$ film. The presence of defect has been confirmed by the Raman study, where we observed an additional D peak (at 252.5 cm^{-1}) due to defects besides the A_{1g} peak for snow-like $MoSe_2$. The temperature-dependent PL study clearly suggests that emission phenomena in $MoSe_2$ nanostructures can be tuned by changing morphologies, which can be used for developing desired atomically thin spintronic and valleytronic devices.

The electron undergoes the transition from an excited state of the recombination centre to the ground state *via* direct or indirect routes. At higher temperatures, radiative transitions are gradually replaced by non-radiative ones comprising the same defects, resulting in PL quenching as suggested by Mott–Seitz model.[30,31] The temperature dependence of PL intensity of the $MoSe_2$ film is shown in Fig. 3b and e and can be expressed as follows-

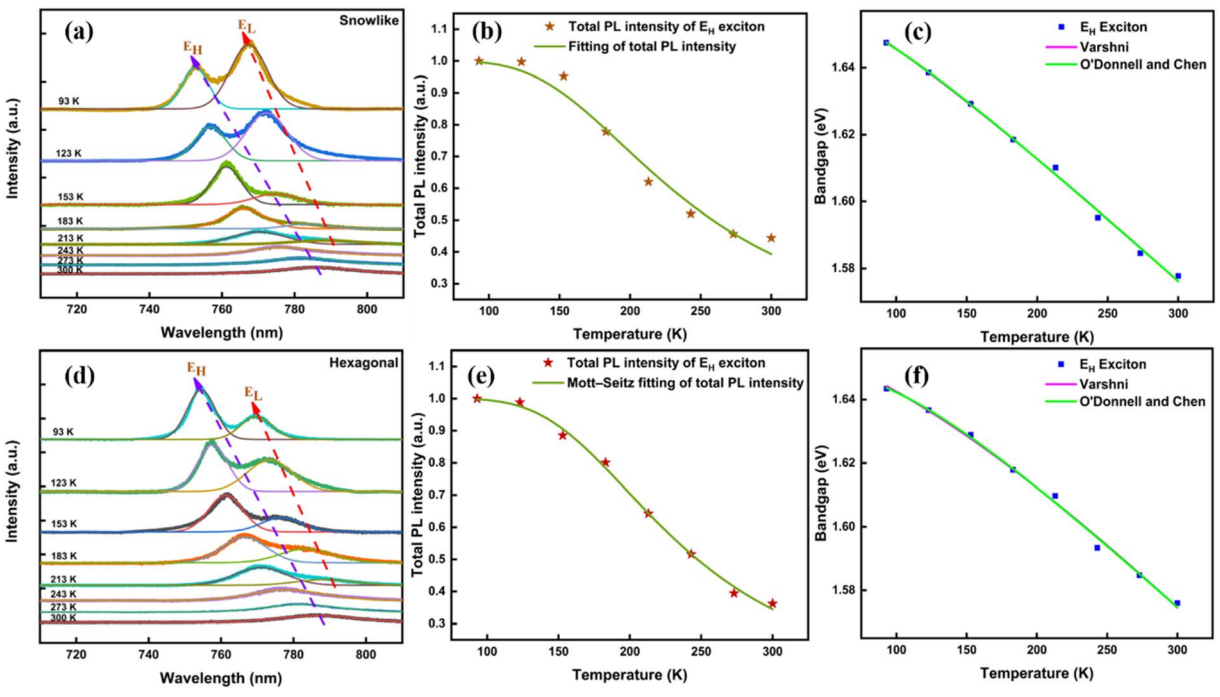

Fig. 3 Gaussian fitted PL spectra in the temperature range 93–300 K for (a) snow-like and (d) hexagonal $MoSe_2$; variation of total PL intensity for E_H exciton with temperature (b) snow-like and (e) hexagonal $MoSe_2$; and fitting of variation in bandgap with temperature for (c) snow-like and (f) hexagonal $MoSe_2$ film.

$$I(T) = \frac{1}{1 + A\exp\left(-\frac{E_a}{k_B T}\right)} \quad (3)$$

where $I(T)$ is the PL intensity at a given temperature T, A is known as a ratio of the nonradiative to radiative transitions probability, E_a is the activation energy for nonradiative recombination and k_B is the Boltzmann constant. The configuration coordinate diagram is provided in Fig. S4 of the ESI,† which comprises thermally induced excitation of the defect to the level at which adiabatic potentials of its ground and excited states cross, followed by nonradiative transition leading to phonon emission. The energy separation between the potential minimum of the excited state and the cross-over point of the excited and ground states provides the activation energy (E_a). The obtained values of A and E_a for snow-like and hexagonal $MoSe_2$ are summarized in Table 1. The lattice expansion along with increased phonon–phonon and electron–phonon interactions leads to the reduced intensity and red shifting of PL peaks with increasing temperature. The red-shift of E_H excitons with temperature for prepared snow-like and hexagonal $MoSe_2$ on SiO_2/Si substrate is shown in Fig. 3c and f, respectively. This behaviour follows the Varshni and the O'Donnell and Chen models.[32,33] The modified Varshni equation can be expressed as follows-

$$E_g(T) = E_g(0) - \frac{\alpha T^2}{(T + \beta)} \quad (4)$$

where $E_g(T)$ and $E_g(0)$ represent the energy of E_H exciton at temperature T and 0 K, respectively. The α and β are Varshni coefficients related to the temperature-dependent dilation of lattice and electron–phonon interaction. The obtained values of $E_g(0)$ and Varshni coefficients of high energy exciton for snow-like and hexagonal $MoSe_2$ are given in Table 1.

We further fit the variation of bandgap using an additional formula, known as the O'Donnell and Chen equation to obtain the electron–phonon coupling constant (S) and the average energy of the phonon $\langle\hbar\omega\rangle$. This equation can be expressed as follows-

$$E_g(T) = E_g(0) - S\langle\hbar\omega\rangle\left[\coth\left(\frac{\hbar\omega}{2k_B T}\right) - 1\right] \quad (5)$$

The obtained values of $E_g(0)$, S, and $\hbar\omega$ for snow-like and hexagonal $MoSe_2$ are given in Table 1. Similar values of $E_g(0)$ for both morphologies are obtained using eqn (4) and (5). The higher values of coupling constant 'S' and average phonon energy '$\langle\hbar\omega\rangle$' for hexagonal $MoSe_2$ compared to snow-like $MoSe_2$ show a greater extent of phonon interaction with E_H exciton in hexagonal $MoSe_2$. The enhanced phonon–exciton interaction and lattice expansion with increasing temperature led to the linear increase of full width at half maximum (FWHM) for E_H exciton, as shown in Fig. S5 of the ESI.† In summary, the temperature-dependent PL study of $MoSe_2$ clearly suggests that the low energy excitons are predominant in snow-like $MoSe_2$ due to the presence of defects and the electron–phonon coupling is stronger in hexagonal $MoSe_2$. This study also indicates the tunability of bandgap in $MoSe_2$ with morphology and external physical stimuli-like temperature.

Table 1 Fitting parameters related to thermal response of high energy excitons (E_H) for snow-like and hexagonal $MoSe_2$

Parameter	Snow-like $MoSe_2$	Hexagonal $MoSe_2$
Mott–Seitz equation		
E_a (meV)	69.64	77.98
A	22.86	38.91
Varshni's equation		
E_0 (eV)	1.66	1.65
α (10^{-4} eV K^{-1})	4.03	5.11
β (K)	108.35	260.52
O'Donnell's equation		
E_0 (eV)	1.65	1.64
S	2.24	2.38
$\langle\hbar\omega\rangle$ (meV)	17.06	25.83

Thermal transport behaviour of $MoSe_2$ nanostructures

To evaluate the thermal conductivity and interfacial thermal conductance of snow-like and hexagonal $MoSe_2$ thin film on a SiO_2/Si substrate, we performed the optothermal Raman technique, which includes temperature and laser power-dependent Raman studies.[17,33] In a temperature-dependent Raman study, the Raman shift is utilized to inspect the electron–phonon and phonon–phonon interactions. The temperature-dependent Raman study was performed using the LWD 50× objective lens in the temperature range 93–300 K. The temperature-dependent Raman spectra for snow-like and hexagonal $MoSe_2$ films over the SiO_2/Si substrate at different temperatures are shown in Fig. 4a and c, respectively. The remaining Lorentzian-fitted Raman spectra at other temperatures are provided in Fig. S6 of the ESI.† The corresponding variations in the peak position of A_{1g} modes for both morphologies of the $MoSe_2$ film with temperature are shown in Fig. 4b and d. Their linear and non-linear responses are analyzed using the following eqn (6) and (7). The linear dependence can be expressed as follows-

$$\omega(T) = \omega_0 + \chi_T T \quad (6)$$

where $\omega(T)$ and ω_0 are the frequencies of the Raman mode at any temperature (T) and at 0 K, respectively, while slope χ_T is the first-order thermal coefficient. The corresponding χ_T values for snow-like and hexagonal $MoSe_2$ are found to be $-(0.0096 \pm 0.0004)$ and $-(0.0115 \pm 0.0002)$ cm^{-1} K^{-1}, respectively. The thermal response of A_{1g} mode for snow-like $MoSe_2$ is found non-linear, while for hexagonal $MoSe_2$ it is found to be more linear in nature.

The non-linear thermal response of snow-like $MoSe_2$ obeys the following second-order polynomial function, consisting of first- and second-order thermal coefficients (χ_1, χ_2).[34]

$$\omega(T) = \omega_0 + \chi_1 T + \chi_2 T^2 \quad (7)$$

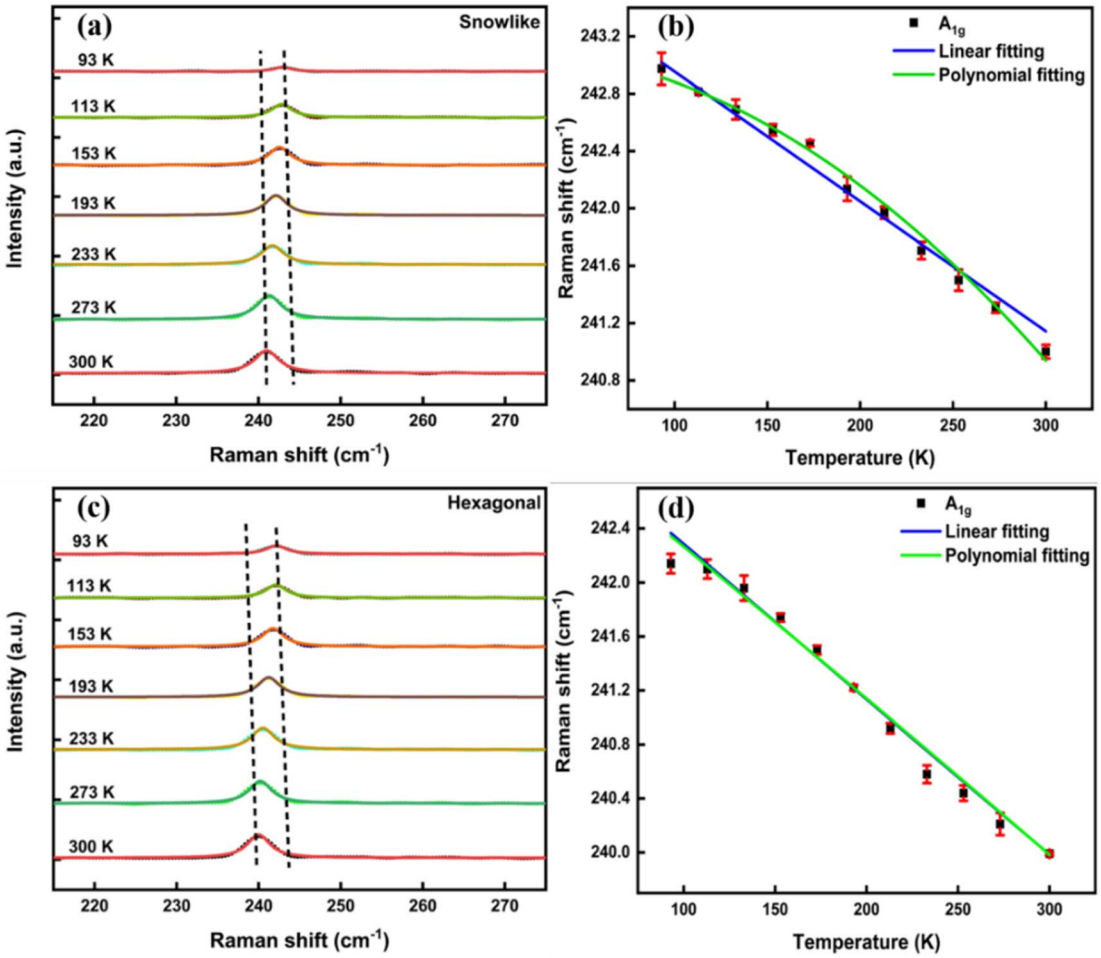

Fig. 4 Temperature-dependent Raman spectra of (a) snow-like and (c) hexagonal $MoSe_2$; Raman shifts with temperature in (b) snow-like and (d) hexagonal $MoSe_2$ using LWD 50× objective lens.

The polynomial fit is found better for snow-like $MoSe_2$ suggesting that the anharmonic effect of phonon–phonon coupling is the main cause of the nonlinear thermal response of Raman mode in snow-like $MoSe_2$. The nonlinear thermal response of $MoSe_2$ can be quantitatively evaluated using a semi-quantitative model by taking two effects into account. The first effect is the pure volume effect arising from the lattice thermal expansion and the second effect is the pure temperature effect resulting from three- and four-phonon scattering processes in phonon–phonon interaction. This semi-quantitative model can be expressed as follows-[35,36]

$$\omega(T) = \omega_0 + \Delta\omega_A + \Delta\omega_E \quad (8)$$

where $\Delta\omega_E$ and $\Delta\omega_A$ denote the Raman shifts arising from pure volume and pure temperature effects, respectively. The effect of volume expansion on Raman shift can be explained by the following Gruneisen constant model.[35,36]

$$\Delta\omega_E(T) = \omega_0 \exp\left(-n\gamma \int_0^T \alpha_T dT\right) - \omega_0 \quad (9)$$

where n is the degeneracy, and its value in the A_{1g} mode for $MoSe_2$ is 1. The thermal expansion coefficient of the materials is denoted by α_T, while γ is the Gruneisen parameter. The integral shows the decrease in vibration frequency with volume expansion. The value of ω_0 is found by linear fitting. Additionally, the product $\gamma\alpha_T$ of the $MoSe_2$ nanostructure is given in the form of the following polynomial expression.[35,36]

$$\gamma\alpha_T = a + bT + cT^2 \quad (10)$$

where a, b, and c are the fitting constants. The anharmonic impact of three- and four-phonon scattering processes is the primary cause of the pure temperature effect comprising different light–matter interactions such as photon absorption, emission, and scattering. The semiquantitative model, developed by Klemens, expresses the pure temperature effect as follows-[37]

$$\Delta\omega_A(T) = A\left(1 + \frac{2}{e^x - 1}\right) + B\left(1 + \frac{3}{e^y - 1} + \frac{3}{(e^y - 1)^2}\right) \quad (11)$$

where, $x = \frac{\hbar\omega}{2k_BT}$ and $y = \frac{\hbar\omega}{3k_BT}k_B$ is the Boltzmann constant, T is the temperature (in kelvin), while coefficients A and B denote the separate contributions of the three- and four-phonon processes, respectively.

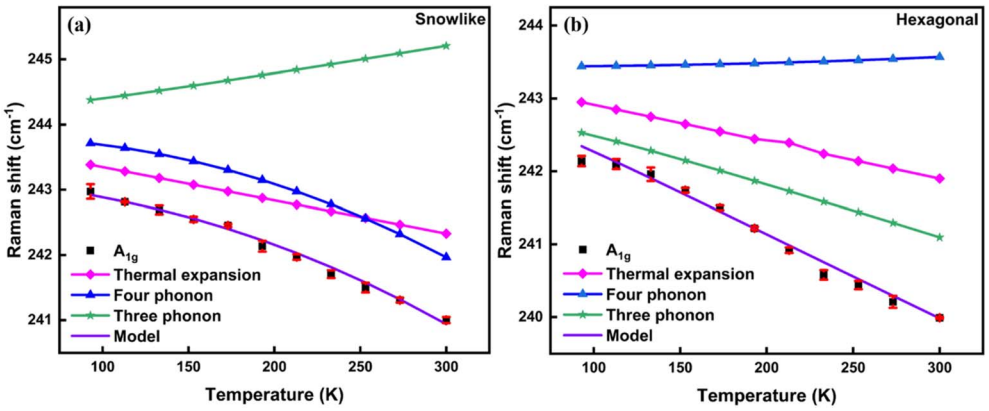

Fig. 5 The simulation of the temperature dependence of Raman shift considering the individual contributions from the processes of thermal expansion, three-phonon, and four-phonon scatterings for (a) snow-like; and (b) hexagonal $MoSe_2$ film.

The nonlinear temperature dependency of Raman shifts is then fitted using eqn (8)–(11) as was done in our recent study on MoS_2.[38] The contributions from the processes of thermal expansion, three-phonon, and four-phonon scatterings for both the morphologies of $MoSe_2$ are shown in Fig. 5. The A and B fit parameters can be extracted by nonlinear temperature response. The retrieved fitting parameters are $A = 0.38357$, $B = -0.0405$ for snow-like $MoSe_2$ and $A = -0.66297$, $B = 0.00289$ for the hexagonal $MoSe_2$ film. Here, $\gamma = 0.2$ as the Gruneisen parameter and thermal expansion coefficient $\alpha_T = 10.5 \times 10^{-5}$ K^{-1} are taken for A_{1g} mode of $MoSe_2$ from literature.[39,40] In Fig. 5, the observed experimental data are displayed along with the predicted temperature-dependent phonon profiles, *i.e.*, contributions of thermal expansion, three- and four-phonon scattering processes for the A_{1g} mode of snow-like (Fig. 5a), and hexagonal (Fig. 5b) $MoSe_2$ film. The non-linear temperature dependence of the Raman shift for snow-like $MoSe_2$ can be explained by the four-phonon process at low temperatures, with thermal expansion mostly acting as a weak linear temperature-dependent component. This study clearly suggests that the anharmonic effect arising from the four-phonon process is the primary cause of the non-linear temperature dependency in snow-like $MoSe_2$, while the three-phonon process is mainly responsible for the non-linear temperature response of hexagonal $MoSe_2$. The CVD-grown $MoSe_2$ film showed a higher degree of non-linearity in the Raman shift due to the presence of defects and chemically active sites. The probability of higher-order phonon scattering is increased as the defect increases. The four-phonon process is dominant in snow-like $MoSe_2$ due to the additional presence of defects associated with Se vacancy. In summary, the shift in the Raman modes with temperature for both morphologies of 3L-$MoSe_2$ film over the SiO_2/Si substrate can be attributed to the thermal expansion of the crystal and the resulting anharmonicity of phonon modes. The shifts in phonon energies occur due to the lattice contraction or expansion with temperature variation resulting in the change of atomic mean positions and interatomic forces. Consequently, phonon shift with temperature can be utilized to observe local temperature evolution in the synthesized semiconducting $MoSe_2$ film by measuring the change in A_{1g} Raman mode. The linear increase of FWHM for the A_{1g} mode with increasing temperature is shown in Fig. S6 of the ESI,† suggesting the softening of the mode in both morphologies of $MoSe_2$. Hence, our study suggests that phonon confinement in the $MoSe_2$ film is extremely sensitive to thermal energy, signifying its better thermal transport behaviour, which can play a vital role in $MoSe_2$-based devices.

Power-dependent Raman study

In order to calculate the thermal conductivity of SiO_2/Si substrate-supported snow-like and hexagonal 3L-$MoSe_2$, we studied their phonon confinement behaviour in response to a local rise in temperature by laser heating with different laser powers. Raman spectra collected at different laser powers using the LWD 50× objective lens are shown in Fig. 6a and c for snow-like and hexagonal $MoSe_2$, respectively, and the linear response of their corresponding Raman shifts with laser powers are shown in Fig. 6b and d, respectively. An enhancement in the intensity of the A_{1g} mode due to increasing incident light intensity and red shift was observed with increasing laser power due to the softening of bonds *via* local temperature rise in $MoSe_2$. Raman spectra at different laser power using a 100× objective lens are shown in Fig. S7 of the ESI.† The linear Raman shift in power-dependent Raman spectra can be described as follows-

$$\omega(P) = \omega_0 + \chi_P P \quad (12)$$

where P is incident laser power at the sample and the slope $\chi_P = \frac{\delta\omega}{\delta P}$ is a first-order power-dependent coefficient. The χ_P values are found to be $-(0.4797 \pm 0.0150)$ and $-(0.8307 \pm 0.0801)$ cm^{-1} mW^{-1} for snow-like and hexagonal $MoSe_2$, respectively, using LWD 50× lens and in the case of 100× lens χ_P values are $-(0.4919 \pm 0.0234)$ and $-(1.2236 \pm 0.1367)$ cm^{-1} mW^{-1} for snow-like and hexagonal $MoSe_2$, respectively. In addition to the Raman shift with laser power, we also noticed the linear increase in FWHM with laser heating, as shown in

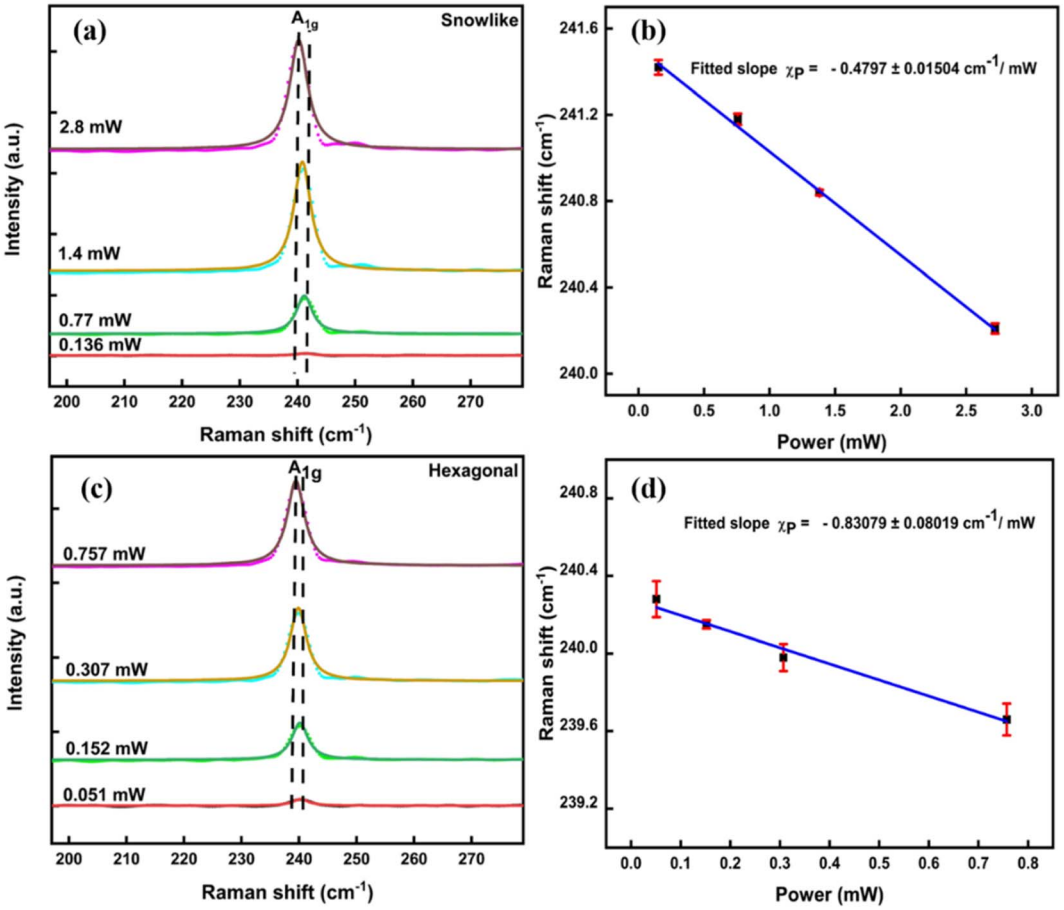

Fig. 6 Lorentzian fitted power-dependent Raman spectra for (a) snow-like and (c) hexagonal $MoSe_2$ and (b and d) their corresponding Raman shifts with incident laser power, using the LWD 50× objective lens.

Fig. S8 of the ESI.† The increase in FWHM and observed red shift in the A_{1g} mode with increasing laser power can be directly ascribed to the lattice expansion and softening of bonds.

We have extracted the interfacial thermal conductance per unit area (g) and thermal conductivity (k_s) of the synthesized $MoSe_2$ film over the SiO_2/Si substrate using the strategy from our earlier report on thermal conductivity of MoS_2.[33] Thermal conduction through $MoSe_2$ film over the SiO_2/Si substrate can be described by following heat diffusion eqn (13) in the form of cylindrical coordinate.[41,42]

$$\frac{1}{r}\frac{\mathrm{d}}{\mathrm{d}r}\left(r\frac{\mathrm{d}T(r)}{\mathrm{d}r}\right) - \frac{g}{t\times k_s}(T(r)-T_{\mathrm{amb}}) = -\frac{Q}{k_s} \qquad (13)$$

where $T(r)$ is the radial temperature distribution, T_{amb} is the global ambient temperature and r is the distance measured from centre of the laser beam. Here, t is the thickness of synthesized $MoSe_2$ film, k_s is the in-plane thermal conductivity of the SiO_2/Si supported $MoSe_2$ film, g is the total interfacial thermal conductance per unit area between the film and the substrate, and Q is the volumetric optical heating power density. This equation has been solved using our developed MATLAB simulation, as described in our earlier reports.[33,38] The solution provides an expression for R_m depending on the ratio of g and k_s, while two R_m values are obtained by different laser spot sizes using two distinct objective lenses 100× and LWD 50× to obtain the final value of g and k_s. We calculated the radius of the laser beam spot size for 100× and LWD 50× objective lenses to be around 0.19 and 0.28 μm, respectively, a detailed calculation is provided in Section S8 of the ESI.† Experimentally the value of thermal resistance (R_m) of the synthesized $MoSe_2$ film can be calculated *via* the following relation-

$$R_m = \frac{\chi_P}{\alpha_a \chi_T} \qquad (14)$$

where, the absorption coefficient $\alpha_a \sim 0.161$ for trilayer $MoSe_2$, details calculation is provided in the Section S9 of the ESI.† For the snow-like $MoSe_2$ film, we found the experimental value of $R_m = 3.8521 \times 10^5$ and 3.2886×10^5 KW^{-1} for the spot size 0.19 μm (objective lens 100×) and 0.28 μm (objective lens LWD 50×), respectively and for the hexagonal $MoSe_2$ film, the experimental value of $R_m = 6.6086 \times 10^5$ and 4.4871×10^5 KW^{-1} for the spot size 0.19 and 0.28 μm, respectively. We determined the value of $g \sim 6.0788 \pm 1.3707$ MW m^{-2} K^{-1} and $k_s \sim 36 \pm 6$ W m^{-1} K^{-1} for snow-like $MoSe_2$ and $g \sim 3.2278 \pm 0.58565$ MW m^{-2} K^{-1} and $k_s \sim 41 \pm 7$ W m^{-1} K^{-1} for hexagonal $MoSe_2$, by solving the MATLAB simulation. The decrease in phonon group velocity induced by defects, as well as phonon localization at atomic-scale lattice defects results in lower thermal conductivity of

Table 2 Thermal conductivity of 2D materials by the optothermal Raman method

2D materials	Raman mode	k_s (W m^{-1} K^{-1})	Reference
200 nm-graphene (supported SiO_2/Si)	G	370 + 650/−320	41
4 nm-PtS_2 (suspended)	E_g	85.6 ± 7.70	43
4.5 nm-$PtSe_2$ (suspended)	E_g	40.4 ± 4.67	43
5 to 15L-$SnSe_2$ (suspended)	A_{1g}	1.80–2.90	44
2L-MoS_2 (supported SiO_2/Si)	A_{1g}	42 ± 8	33
2L-MoS_2 (supported Au–SiO_2/Si)	A_{1g}	35 ± 7	16
2L-$MoSe_2$ (supported Au–SiO_2/Si)	A_{1g}	17 ± 4	16
Snow-like 3L-$MoSe_2$ (supported SiO_2/Si)	A_{1g}	36 ± 6	This work
Hexagonal 3L-$MoSe_2$ (supported SiO_2/Si)	A_{1g}	41 ± 7	This work

snow-like $MoSe_2$ compared to the hexagonal $MoSe_2$. Additionally, the contribution of low-frequency phonons declines with increasing defects as a result of enhanced coupling between low-frequency and high-frequency phonons. The interfacial thermal conductance of the snow-like $MoSe_2$ film is found higher due to the presence of additional Se vacancy defects. Table 2 summarizes the comparison of our findings on the optothermal Raman measurements for thermal conductivity of 3L-$MoSe_2$ with other reports on different 2D materials. It clearly shows that our prepared 3L-$MoSe_2$ on SiO_2/Si substrate shows significant thermal conductivity for both morphologies making them suitable for thermal transport in optoelectronic devices. The semiconducting response of such optoelectronic devices can be tuned by using different morphology of $MoSe_2$ and/or applying different temperatures.

Conclusions

In conclusion, we synthesized two different morphologies (snow-like and hexagonal) of 3L-$MoSe_2$ over SiO_2/Si substrate *via* the CVD technique. We reported for the first time morphological dependent phonon confinement behaviour of $MoSe_2$ at low temperatures, revealing that the defect-bound excitons (E_L) are more dominant in snow-like $MoSe_2$ compared to hexagonal $MoSe_2$ due to the presence of additional defects in snow-like $MoSe_2$ film. We also demonstrated morphological-dependent thermal transport properties of $MoSe_2$ for the first time to the best of our knowledge. We observed that four phonon scattering process is dominant in snow-like $MoSe_2$ for thermal transport in comparison to three phonon process in hexagonal $MoSe_2$. We also observed the thermal conductivity (k_s) $\sim 36 \pm 6$ W m^{-1} K^{-1} and interfacial thermal conductance (g) $\sim 6.0788 \pm 1.3707$ MW m^{-2} K^{-1} for snow-like $MoSe_2$ film and $k_s \sim 41 \pm 7$ W m^{-1} K^{-1} and $g \sim 3.2278 \pm 0.5856$ MW m^{-2} K^{-1} for hexagonal $MoSe_2$ film. The higher-order phonon scattering in snow-like $MoSe_2$ results in lower thermal conductivity and higher interfacial thermal conductance compared to hexagonal $MoSe_2$. Our study paves the way for developing $MoSe_2$ based externally modulated optoelectronic device by tuning its morphology.

Author contributions

Jay Deep Gupta was involved in the idea of the project, the synthesis of material, analysing data, and writing the manuscript. Priyanka Jangra was involved in the investigation of DFT calculation. Bishnu Pada Majee was involved in the optothermal study. Ashish Kumar Mishra was involved in the supervision and administration of the project, arrangement of resources, data analysis, review, and editing of the manuscript.

Conflicts of interest

The authors declare that they have no known competing financial interests or personal relationships that could have appeared to influence the work reported in this paper.

Acknowledgements

The authors thank IIT (BHU) and its Central Instrument Facility. JDG is thankful to the Ministry of Education, Govt. of India for the Prime Minister Research Fellowship (PMRF). AKM acknowledges the support of SERB, India (Grant No. CRG/2020/002186). The authors also thank Dr Abhishek Sanskrityayn for the discussion on the mathematical model.

References

1 X. Song, Z. Guo, Q. Zhang, P. Zhou, W. Bao and D. W. Zhang, *Small*, 2017, **13**, 1700098.
2 Q. H. Wang, K. Kalantar-Zadeh, A. Kis, J. N. Coleman and M. S. Strano, *Nat. Nanotechnol.*, 2012, **7**, 699–712.
3 C. Chakraborty, N. Vamivakas and D. Englund, *Nanophotonics*, 2019, **8**, 2017–2032.
4 S. I. Azzam, K. Parto and G. Moody, *Appl. Phys. Lett.*, 2021, **118**, 240502.
5 Z. Shi, H. Zhang, K. Khan, R. Cao, K. Xu and H. Zhang, *Nano Res.*, 2022, **15**, 104–122.
6 H. Lee, J. Ahn, S. Im, J. Kim and W. Choi, *Sci. Rep.*, 2018, **8**, 1–7.
7 S. Sotgiu, T. Venanzi, F. Macheda, E. Stellino, M. Ortolani, P. Postorino and L. Baldassarre, *Phys. Rev. B*, 2022, **106**, 085204.
8 N. Kumar, J. He, D. He, Y. Wang and H. Zhao, *Nanoscale*, 2014, **6**, 12690–12695.
9 X. Wang, Y. Gong, G. Shi, W. L. Chow, K. Keyshar, G. Ye, R. Vajtai, J. Lou, Z. Liu, E. Ringe, B. K. Tay and P. M. Ajayan, *ACS Nano*, 2014, **8**, 5125–5131.
10 S. Ren, Q. Tan and J. Zhang, *J. Semicond.*, 2019, **40**, 071903.

11 Y. Liu, Y. Liu, H. Zhou, Z. Yang, Y. Qu, Y. Tan and F. Chen, *ACS Nano*, 2021, **15**, 16572–16580.
12 D. Saleta Reig, S. Varghese, R. Farris, A. Block, J. D. Mehew, O. Hellman, P. Woźniak, M. Sledzinska, A. el Sachat, E. Chávez-Ángel, S. O. Valenzuela, N. F. Van Hulst, P. Ordejón, Z. Zanolli, C. M. Sotomayor Torres, M. J. Verstraete and K. J. Tielrooij, *Adv. Mater.*, 2022, **34**, 2108352.
13 A. Kandemir, H. Yapicioglu, A. Kinaci, T. Çağin and C. Sevik, *Nanotechnology*, 2016, **27**, 055703.
14 Y. Hong, J. Zhang and X. C. Zeng, *J. Phys. Chem. C*, 2016, **120**, 26067–26075.
15 H. Zobeiri, R. Wang, T. Wang, H. Lin, C. Deng and X. Wang, *Int. J. Heat Mass Transfer*, 2019, **133**, 1074–1085.
16 X. Zhang, D. Sun, Y. Li, G. H. Lee, X. Cui, D. Chenet, Y. You, T. F. Heinz and J. C. Hone, *ACS Appl. Mater. Interfaces*, 2015, **7**, 25923–25929.
17 J. Sun, K. Dai, W. Xia, J. Chen, K. Jiang, Y. Li, J. Zhang, L. Zhu, L. Shang, Z. Hu and J. Chu, *ACS Omega*, 2021, **6**, 30526–30533.
18 J. Li, W. Yan, Y. Lv, J. Leng, D. Zhang, C. O. Coileaín, C. P. Cullen, T. Stimpel-Lindner, G. S. Duesberg, J. Cho, M. Choi, B. S. Chun, Y. Zhao, C. Lv, S. K. Arora and H. C. Wu, *RSC Adv.*, 2020, **10**, 1580–1587.
19 J. Wang, X. Cai, R. Shi, Z. Wu, W. Wang, G. Long, Y. Tang, N. Cai, W. Ouyang, P. Geng, B. N. Chandrashekar, A. Amini, N. Wang and C. Cheng, *ACS Nano*, 2018, **12**, 635–643.
20 W. Zheng, Y. Qiu, W. Feng, J. Chen, H. Yang, S. Wu, D. Jia, Y. Zhou and P. Hu, *Nanotechnology*, 2017, **28**, 395601.
21 M. Cowie, R. Plougmann, Y. Benkirane, L. Schué, Z. Schumacher and P. Grütter, *Nanotechnology*, 2022, **33**, 125706.
22 Z. Gan, E. Najafidehaghani, S. H. Han, S. Shradha, F. Abtahi, C. Neumann, J. Picker, T. Vogl, U. Hübner, F. Eilenberger, A. George and A. Turchanin, *Small Methods*, 2022, **6**, 2200300.
23 M. Mahjouri-Samani, L. Liang, A. Oyedele, Y. S. Kim, M. Tian, N. Cross, K. Wang, M. W. Lin, A. Boulesbaa, C. M. Rouleau, A. A. Puretzky, K. Xiao, M. Yoon, G. Eres, G. Duscher, B. G. Sumpter and D. B. Geohegan, *Nano Lett.*, 2016, **16**, 5213–5220.
24 J. Xia, X. Huang, L. Z. Liu, M. Wang, L. Wang, B. Huang, D. D. Zhu, J. J. Li, C. Z. Gu and X. M. Meng, *Nanoscale*, 2014, **6**, 8949–8955.
25 S. Tongay, J. Zhou, C. Ataca, K. Lo, T. S. Matthews, J. Li, J. C. Grossman and J. Wu, *Nano Lett.*, 2012, **12**, 5576–5580.
26 Y. Sun, D. Wang and Z. Shuai, *J. Phys. Chem. C*, 2016, **120**, 21866–21870.
27 L. Xu, L. Zhao, Y. Wang, M. Zou, Q. Zhang and A. Cao, *Nano Res.*, 2019, **12**, 1619–1624.
28 T. Godde, D. Schmidt, J. Schmutzler, M. Aßmann, J. Debus, F. Withers, E. M. Alexeev, O. del Pozo-Zamudio, O. V. Skrypka, K. S. Novoselov, M. Bayer and A. I. Tartakovskii, *Phys. Rev. B*, 2016, **94**, 165301.
29 M. A. Reshchikov, *J. Appl. Phys.*, 2014, **115**, 012010.
30 N. F. Mott, *Proc. R. Soc. London, Ser. A*, 1938, **167**, 384–391.
31 F. Seitz, *Trans. Faraday Soc.*, 1939, **35**, 74–85.
32 K. P. O'Donnell and X. Chen, *Appl. Phys. Lett.*, 1991, **58**, 2924–2926.
33 B. P. Majee, J. D. Gupta, A. Sanskrityayn and A. K. Mishra, *J. Phys. Chem. C*, 2021, **125**, 14865–14873.
34 Z. Lin, W. Liu, S. Tian, K. Zhu, Y. Huang and Y. Yang, *Sci. Rep.*, 2021, **11**, 1–9.
35 S. Najmaei, P. M. Ajayan and J. Lou, *Nanoscale*, 2013, **5**, 9758–9763.
36 X. T. Huang, Y. Gao, T. Q. Yang, W. C. Ren, H. M. Cheng and T. S. Lai, *Sci. Rep.*, 2016, **6**, 32236.
37 P. G. Klemens, *Phys. Rev.*, 1966, **148**, 845.
38 A. Singh, B. P. Majee, J. D. Gupta and A. K. Mishra, *J. Phys. Chem. C*, 2023, **127**, 3787–3799.
39 D. J. Late, S. N. Shirodkar, U. V. Waghmare, V. P. Dravid and C. N. R. Rao, *ChemPhysChem*, 2014, **15**, 1592–1598.
40 D. Kumar, V. Kumar, R. Kumar, M. Kumar and P. Kumar, *Phys. Rev. B*, 2022, **105**, 085419.
41 W. Cai, A. L. Moore, Y. Zhu, X. Li, S. Chen, L. Shi and R. S. Ruoff, *Nano Lett.*, 2010, **10**, 1645–1651.
42 A. Mohapatra, S. Das, K. Majumdar, M. R. Rao and M. Jaiswal, *Nanoscale Adv.*, 2021, **3**, 1708–1716.
43 S. Yin, W. Zhang, C. Tan, L. Chen, J. Chen, G. Li, H. Zhang, Y. Zhang, W. Wang and L. Li, *J. Phys. Chem. C*, 2021, **125**, 16129–16135.
44 B. Zou, Y. Zhou, X. Zhang, M. Zhang, K. Liu, M. Gong and H. Sun, *ACS Appl. Nano Mater.*, 2020, **3**, 10543–10550.